



Cite this: *J. Mater. Chem. A*, 2023, 11, 13916Received 8th April 2023  
Accepted 9th June 2023

DOI: 10.1039/d3ta02127k

rsc.li/materials-a

# Self-templated synthesis of novel and robust honeycomb-like N-doped highly graphitized carbon from low-temperature carbonization†

Ha-Young Lee, <sup>a</sup> Caleb Gyan-Barimah, <sup>a</sup> Cheol-Hwan Shin <sup>a</sup>  
and Jong-Sung Yu <sup>\*ab</sup>

Graphiticity and porosity are two marvelous properties desired in carbon support materials for electrocatalytically active materials. However, simultaneously incorporating the aforementioned properties is deemed incompatible with thermally induced carbon synthesis. A unique approach to realizing carbon materials with such dual properties at the same time is the use of porogen templates. In this study, g-C<sub>3</sub>N<sub>4</sub> is pyrolyzed with the aid of metallic Mg to produce highly graphitized N-doped carbon endowed with abundant Mg<sub>3</sub>N<sub>2</sub> sites. Notably, the self-generated Mg<sub>3</sub>N<sub>2</sub> in the carbon matrix acts as a template for a unique honeycomb-like porous structure after etching of the porogen. Thus, the honeycomb-like N-doped graphitized carbon (HNGC) is found to be an effective support material for anchoring PtCo alloy nanoparticles which improved the mass transport pathways, resulting in a high peak power density in polymer electrolyte membrane fuel cell (PEMFC) operation. In addition, HNGC's high graphiticity enables it to withstand the harsh conditions of the DOE accelerated durability test (ADT), while the N-doping enhances its mass activity (MA), contributing to excellent support durability and catalytic performance.

Carbon materials have played a prominent role in various electrochemical applications such as electrocatalysis and energy storage because of their good electrical conductivity, high surface area, and low cost.<sup>1,2</sup> These properties of carbon materials can be attributed to three main factors namely; graphiticity, porosity, and heteroatom doping.<sup>3</sup>

The classical synthesis of carbon materials requires high-temperature pyrolysis of carbon precursors above 700 °C in an inert atmosphere.<sup>4</sup> Most importantly, pyrolysis at temperatures >2000 °C is necessary to achieve a highly graphitized structure. Yet, this is achieved at the detriment of porosity and heteroatom

doping concentration.<sup>5,6</sup> Thus, a balance between the three factors mentioned earlier is crucial to attaining high efficiency in electrochemical reactions.

The carbon-based materials have been used as metal-free catalysts for many electrochemical reactions such as oxygen reduction reaction (ORR), hydrogen evolution reaction (HER), and CO<sub>2</sub> reduction reaction (CO<sub>2</sub>RR).<sup>7,8</sup> The activity of metal-free carbon is enhanced by controlling heteroatom doping, morphology, and chemical functionalization.<sup>9</sup> Especially, in ORR, carbon atoms near to pyridinic-N were suggested as active sites, providing two possible reaction pathways; 2 + 2- and 4-electron mechanism.<sup>4</sup>

In practical polymer electrolyte membrane fuel cells (PEMFCs), carbon is generally applied as a support material to disperse Pt-based nanoparticles (NPs). The properties of the carbon support directly impact the catalytic activity and durability of Pt NPs.<sup>10,11</sup> The graphiticity of carbon improves its conductivity and oxidation resistance under the high potential ( $E > 1.44$  V<sub>RHE</sub>) during the start and stop operations of PEMFC.<sup>12,13</sup> Heteroatom dopants such as N,<sup>14–16</sup> S,<sup>17</sup> and P<sup>18</sup> typically exhibit a strong interaction with Pt NPs which subsequently leads to an enhancement in the activity and stability. In addition, mesoporosity (2–50 nm) and macroporosity (>50 nm) facilitate mass transfer and water management in practical PEMFC applications.<sup>19</sup>

Template-assisted carbon synthesis offers a uniform and modifiable porous structure.<sup>20–22</sup> Inorganic templates such as MgO, NaCl, and SiO<sub>2</sub> with unique properties have aided in creating mesopores in the range of 2 to 20 nm. However, the preparation and removal of these templates can be tedious, time-consuming, and expensive, leaving researchers to find alternative template materials. In this respect, self-templated synthesis, where the templates are generated *in situ*, has been identified as a simple and effective route to substitute the cumbersome extra preparation methods.

Herein, we report a novel approach involving the combination of metallic Mg powder and g-C<sub>3</sub>N<sub>4</sub> for the creation of a highly graphitized N-doped carbon material with

<sup>a</sup>Department of Energy Science and Engineering, Daegu Gyeongbuk Institute of Science & Technology (DGIST), Daegu 42988, Republic of Korea

<sup>b</sup>Energy Science and Engineering Research Center, DGIST, Daegu 42988, Republic of Korea. E-mail: jsyu@dgist.ac.kr

† Electronic supplementary information (ESI) available: Experimental procedure and supplementary figures. See DOI: <https://doi.org/10.1039/d3ta02127k>

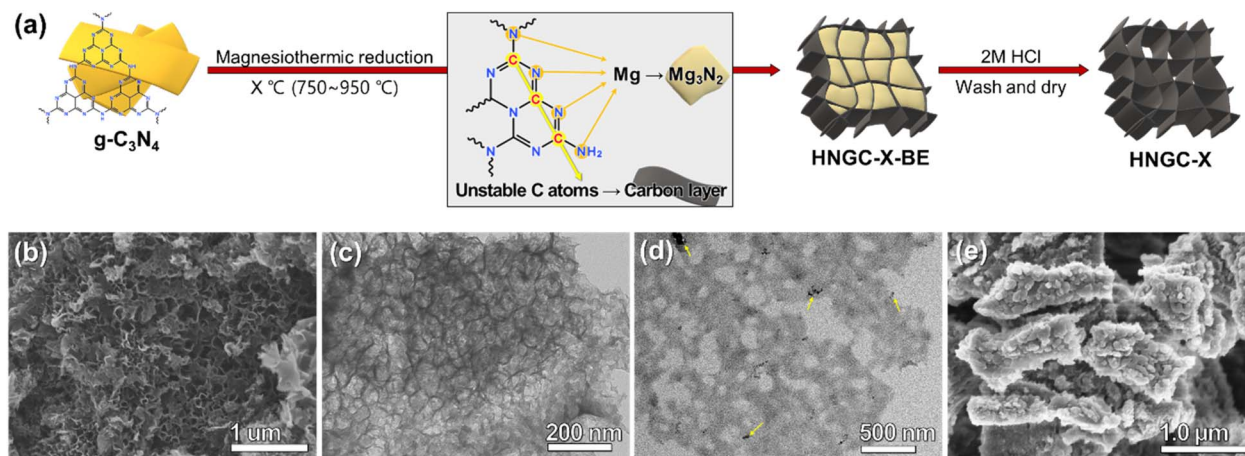


**Fig. 1** (a) Schematic illustration of the mechanism for the preparation of HNGC-X (X stands for the carbonization temperature). (b) SEM and (c) TEM images of HNGC-750. (d) TEM image of microtome sections of epoxy embedded HNGC-750. Black dots (yellow arrow) dispersed over HNGC-750 are epoxy particles for microtome cutting. (e) SEM image for HNGC-750-BE.

a honeycomb-like porous structure created through the etching of *in situ*-generated  $Mg_3N_2$  sites. The honeycomb-like N-doped graphitized carbon (HNGC-X) serves as a support for PGM catalysts in PEMFC. Interestingly, the synchronous N-doping and graphiticity enhanced the ORR kinetics, electrical conductivity, and stability of as-synthesized PtCo NPs.

The formation mechanism for the HNGC-X can be explained from the viewpoint that when metallic Mg powder and  $g-C_3N_4$  are heated together, Mg firstly destabilizes the C–N bonds and takes N atoms from  $g-C_3N_4$  to generate  $Mg_3N_2$  owing to the highly electropositive nature of Mg as illustrated in Fig. 1a.<sup>23,24</sup> Meanwhile, the N-deficient  $g-C_3N_4$  moieties concurrently react together, leading to the formation of highly graphitized carbon layers which are separated by *in situ* generated  $Mg_3N_2$  particles. The  $Mg_3N_2$  particles can then be easily etched out to generate abundant mesopores embedded in the resulting carbon matrix. Thus, the self-generated  $Mg_3N_2$  template provides a honeycomb-like carbon structure. The highly graphitized carbon derived also holds residual N atoms not coordinated with the Mg atoms. This facile synthesis can simultaneously control the three key features desired in carbon materials namely; graphiticity, N-doping, and porosity.

Pristine  $g-C_3N_4$  displays randomly oriented sheet-like morphology in Fig. S1a,† while HNGC-X samples obtained at different annealing temperatures clearly show well-distributed pores on the surface as evidenced in the SEM and TEM images (Fig. 1b, d, S1b and c†). Interestingly, they all exhibit a honeycomb-like porous structure. To investigate the structure of HNGC-750 prepared at 750  $^\circ\text{C}$ , epoxy treatment, and sectioning with ultra-microtome were performed to obtain the cross-section TEM images. Fig. 1c clearly shows mesopores ranging from 20–50 nm. SEM (Fig. 1e) and TEM (Fig. S2†) images for HNGC-750 before acid etching (HNGC-750-BE) demonstrate the existence of small particle-like  $Mg_3N_2$  entities embedded in the carbon matrix, which would leave mesopores in the carbon framework upon etching. The XRD pattern for HNGC-750-BE in Fig. S3† confirms the presence of  $Mg_3N_2$  along

with unreacted Mg. In comparison to the HNGC-750, HNGC-850 and HNGC-950 (Fig. S1b and c†) prepared at 850 and 950  $^\circ\text{C}$  respectively demonstrate much-ordered honeycomb-like porous structures.

$N_2$  adsorption–desorption curves in Fig. 2 and S4† for HNGC-X show a typical Type IV isotherm with a hysteresis loop, representing a mesoporous solid.<sup>25</sup> Table S1† shows that HNGC-X has a high mesopore volume, 1.12–1.51  $\text{cm}^3 \text{g}^{-1}$ , with high surface areas, while showing low micropore volume of less than 0.01  $\text{cm}^3 \text{g}^{-1}$ . The BET surface area of  $g-C_3N_4$  is only 80.8  $\text{m}^2 \text{g}^{-1}$  and dramatically increases to 320.4  $\text{m}^2 \text{g}^{-1}$  after the Mg-aided carbonization at 750  $^\circ\text{C}$ . This signifies that Mg plays a dual role as a reducing agent to convert the carbon precursor to graphitized carbon and as a precursor for the formation of  $Mg_3N_2$ , which works as a new templating agent for the generation of mesopores and macropores. The pore size ranging between 5–35 nm increases in the pore size distribution. The

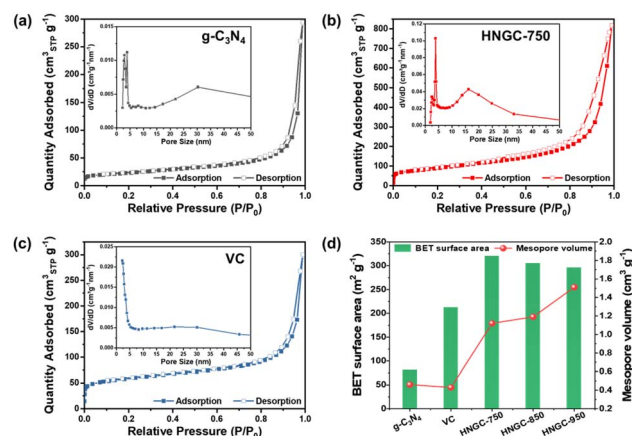


**Fig. 2**  $N_2$  gas adsorption–desorption curves and the corresponding pore size distribution of (a)  $g-C_3N_4$ , (b) HNGC-750, and (c) VC (Vulcan XC 72R). (d) Comparison of BET surface and mesopore volume from VC and as-prepared samples.

BET surface area decreases with an increase in the treatment temperature owing to the decrease in micropore volume (Fig. 2d and Table S1†). All the HNGC-X samples possess a higher BET surface area and mesopore volume than commercial Vulcan XC 72R carbon (VC).

In Fig. 3a the as-prepared HNGC-X samples show a strong graphitic peak at 2-theta angle of  $26^\circ$  in the X-ray diffraction (XRD) patterns. Similarly, in the Raman spectra (Fig. 3b) the G-band peak at  $\sim 1583\text{ cm}^{-1}$  is much higher than the D-band peak for all the HNGC-X samples, demonstrating the formation of a highly graphitized structure. In contrast, the  $\text{g-C}_3\text{N}_4$  exhibits XRD peaks at approximately  $\sim 12.8^\circ$  and  $27.5^\circ$  corresponding to the (001) and (002) planes, respectively.<sup>26</sup> The HNGC-750 exhibits a well-developed graphitic structure as confirmed by  $I_{\text{D}}/I_{\text{G}}$  and  $I_{2\text{D}}/I_{\text{G}}$  values of 0.52 and 1.21, respectively (see Table S2† for other samples). Interestingly, all the HNGC-X samples show a strong 2D band at  $2696\text{ cm}^{-1}$ . Such 2D peaks are only observed in highly graphitized carbon with low lattice defects. This observation signifies that when the heating temperature increases, the G and 2D Raman signals increase accordingly and become narrower (Fig. 3b and Table S2†). Also, the full width at half maximum (FWHM) of the 2D peak lessens at higher temperatures, indicating a decrease in the number of stacked carbon layers.<sup>27</sup> On the other hand, the XRD pattern coupled with the Raman spectrum (Fig. S5†) recorded for the commercial carbon (VC) shows a broad peak at  $\sim 24^\circ$ , corresponding to the (002) plane of amorphous carbon. Additionally, the low  $I_{\text{D}}/I_{\text{G}}$  value (1.00) and the absence of a significant 2D signal indicate a much lower level of graphiticity than the HNGC-X samples.

We also deduced that the amount of Mg and the annealing temperature adopted in the synthesis process affects the nature of the porous structure and the degree of graphitization in the

resulting carbon. In our experiment, 2.0 g of Mg was mixed with 2.0 g of  $\text{g-C}_3\text{N}_4$ , which gives a near 1 : 1 molar ratio between the N in  $\text{g-C}_3\text{N}_4$  (0.087 mol) and Mg (0.082 mol). This equimolar ratio is important to prevent the thermal decomposition of  $\text{g-C}_3\text{N}_4$  to small  $\text{C}_x\text{N}_y$  fragments. As control experiments, 2.0 g of  $\text{g-C}_3\text{N}_4$  was treated with different amounts of Mg such as 0.5, 1.5, and 4.0 g. In the XRD patterns presented in Fig. S6a,† the sample prepared with 0.5 g of Mg (HNGC-750-0.5Mg) exhibits a broad peak at 2-theta angle of  $\sim 23^\circ$  which is associated with amorphous carbon. Furthermore, the Raman spectra in Fig. S6b† show a higher D band and weaker 2D band signals in comparison to the HNGC-750 sample synthesized with 2 g of Mg, signifying a low graphiticity. Interestingly, HNGC-750-4Mg exhibits  $I_{\text{D}}/I_{\text{G}}$  and  $I_{2\text{D}}/I_{\text{G}}$  values (Table S2†) similar to HNGC-750, indicating that for the same synthesis conditions, a minimum of 2.0 g of Mg is necessary to derive the fully graphitized structure. In addition, the SEM image for HNGC-750-0.5Mg in Fig. S7a† shows uneven sheet-like morphology similar to that of the pristine  $\text{g-C}_3\text{N}_4$  in Fig. S1a.† The mesoporous structure gradually develops as the Mg content is increased to 1 g (HNGC-750-1Mg in Fig. S7b and Table S1†). Thus, a 1 : 1 weight ratio between Mg and  $\text{g-C}_3\text{N}_4$  is the minimum requirement to achieve the honeycomb-like mesoporosity as well as the highly graphitic structure.

To determine the atomic composition of HNGC-X, X-ray photoelectron spectroscopy (XPS, technical uncertainty range  $\pm 5\%$ ) was conducted and the results are illustrated in Fig. S8.† The high-resolution C 1s XPS spectra for all HNGC-X samples exhibit the characteristic carbon peak at binding energies in the proximity of 284.56 eV, corresponding to  $\text{sp}^2$  C from the C=C bond in graphitic carbon (Fig. 3c and S8b†).<sup>28</sup> For  $\text{g-C}_3\text{N}_4$ , the main peak of the C 1s spectrum at 288.17 eV can be assigned to the N-C=N bond.<sup>29</sup> The N contents in HNGC-750 and  $\text{g-C}_3\text{N}_4$  are 2.1 and 51.5 at%, respectively (Table S3†). This result further confirms our initial postulate that Mg takes most of the N atoms from  $\text{g-C}_3\text{N}_4$  and subsequently converts  $\text{g-C}_3\text{N}_4$  to N-doped carbon.<sup>30</sup> The high-resolution N 1s XPS spectrum of HNGC-750 is deconvoluted into four sub-peaks including predominant pyrrolic-N (400.04 eV, 41.6%) along with 28.4% pyridinic-N (398.80 eV), 17.1% graphitic-N (401.40 eV), and 12.9% pyridinic-N oxides (403.20 eV) in Fig. 3d and Table S4.†<sup>28,31</sup> N-doping in porous carbon frameworks synergistically improves the reactivity of the active elements, making them highly desirable for various electrochemical systems.<sup>32,33</sup> Especially, in PEMFC, the pyridinic-N, and pyrrolic-N have been reported to improve the catalytic activity and durability of Pt-based catalysts.<sup>31,34</sup> It is quite interesting to note that the pyrrolic-N is predominant in this system owing to the low carbonization temperature employed. This is in contrast to other literature that reports low contents of pyrrolic-N due to the thermodynamic instability at high temperatures.<sup>14,28</sup> As the temperature increases, the pyrrolic-N decreases, and the pyridinic-N becomes the major N configuration in the HNGC-850 and HNGC-950, as shown in Fig. S8c and Table S4.†

The presence of mesopores and macropores in PEMFC catalysts is beneficial for mass transfer of reactants as well as effective water management. To evaluate the effectiveness of

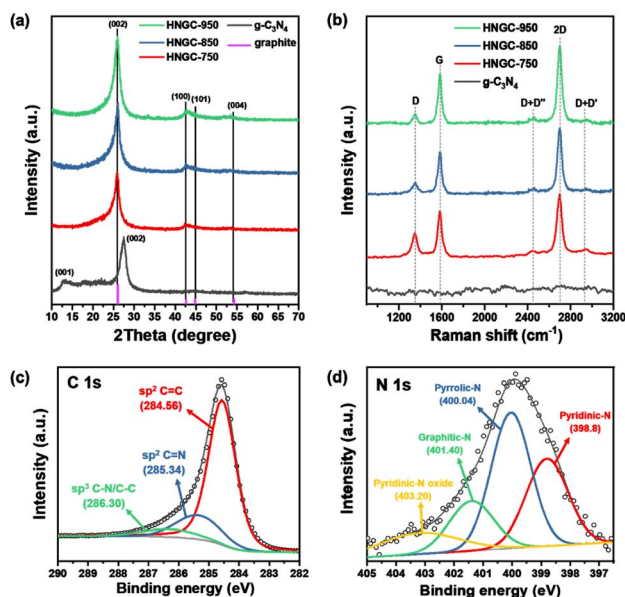


Fig. 3 (a) XRD profiles and (b) Raman spectra for the as-prepared samples. The high-resolution XPS spectrum for (c) C 1s and (d) N 1s for HNGC-750.



HNGC-X as a catalyst support, PtCo was deposited on HNGC-X by microwave-assisted polyol reduction process. For comparison, the same catalyst was deposited on a commercial carbon support, VC. XRD patterns in Fig. S9† show that the diffraction peaks from PtCo are shifted to positive angles relative to the Pt reference (JCPDS card No. 88-2343). As signified by Bragg's law ( $n\lambda = 2d \sin \theta$ ), a decrease in the lattice distance ( $d$ ) increases the diffraction angle. Therefore, the positive shift observed in the PtCo samples is associated with the lattice contraction emanating from the intercalation of Co into the Pt lattice.<sup>35,36</sup> The thermogravimetric analysis (TGA) in Fig. S10b† indicates that all the prepared samples have ~20 wt% of PtCo. Interestingly, the PtCo/HNGC-950 shows the highest onset for carbon oxidation, signifying the higher thermal stability derived from the highly graphitized carbon. The average particle size of PtCo NPs recorded for both carbon supports is approximately 4 nm (Fig. S11a and b†) with similar size distribution. The atomic ratio of Pt to Co in PtCo catalysts was determined by inductively coupled plasma-optical emission spectrometry (ICP-OES) as summarized in Table S5.†

In ORR half-cell tests (Fig. 4a), PtCo/HNGC-750 displays the highest onset, half-wave potential, and diffusion-limited current density among all the prepared samples. All the PtCo/HNGC-X catalysts show better catalytic activity than PtCo/VC. N-doping improves the ORR kinetics by modifying the adsorption strength of oxygenated species.<sup>14,28</sup> In addition, the presence of  $sp^2$ -hybridized N species, such as pyrrolic-N and pyridinic-N, enables additional electrical conductivity derived from lone pair electrons in the perpendicular p-orbital of the N atom.<sup>31,34</sup> Interestingly, the PtCo/HNGC-750 showed better ORR performance compared to PtCo/HNGC-850 and PtCo/HNGC-950

probably due to the higher BET surface area and N concentration of the former.

The membrane electrode assemblies (MEAs) were fabricated with PtCo/VC and PtCo/HNGC-X as cathode electrodes for single-cell tests. PtCo/HNGC-750 among the tested samples delivers the highest mass activity and maximum power density ( $P_{\max}$ ) of  $0.44 \text{ A mg}_{\text{Pt}}^{-1}$  and  $1.54 \text{ W cm}^{-2}$ , respectively in the MEA test under  $\text{H}_2/\text{O}_2$  flow (Fig. 4b, and Table S6†). Furthermore, the HNGC-850 and HNGC-950 in Fig. S12† also displayed a higher performance than PtCo/VC with a mass activity and  $P_{\max}$  of  $0.39 \text{ A mg}_{\text{Pt}}^{-1}$  and  $1.41 \text{ W cm}^{-2}$ , respectively. We postulate that the HNGC-750 provides the optimum synergy required to improve the catalytic activity due to the sufficient N contents, graphiticity, and mesoporosity. Additionally, cell voltages at 0.8 and  $1.5 \text{ A cm}^{-2}$  (Fig. 4d) for PtCo/HNGC-X are higher than PtCo/VC due to the high electrical conductivity. MEAs were also tested under  $\text{H}_2/\text{Air}$  as shown in Fig. 4c. In this condition, PtCo/HNGC-750 shows a higher  $P_{\max}$  than PtCo/VC as summarized in Table S7.† The shape of the polarization curve in the high current density region (Fig. 4c) as well as the cell voltage at  $1.5 \text{ A cm}^{-2}$  (Table S7†) shows that PtCo/HNGC-750 maintains its fuel cell performance very well compared to PtCo/VC in the high current mass transfer region. Clearly, this indicates that the former facilitates mass transport during the PEMFC operation as a result of the honeycomb-like porous structure. The macro- and mesopore volumes offer effective mass transfer in the single cell application.<sup>19,37</sup> The mesopore volume for HNGC-750 is  $1.12 \text{ cm}^3 \text{ g}^{-1}$ , which is 2.6 times higher than the VC value. Thus, the MEA performance of PtCo NPs was improved by the distinctive pore structure of HNGC-750.

Electrochemical impedance spectroscopy (EIS) in Fig. S13† was performed at  $1.0 \text{ A cm}^{-2}$  in  $\text{H}_2/\text{Air}$  condition to verify the mass transport resistance. At  $1.0 \text{ A cm}^{-2}$ , the  $i$ - $V$  curves of PtCo/VC and PtCo/HNGC-750 start to diverge owing to the effect of mass transport resistance. The Nyquist plots of MEAs consist of two arcs; a large diameter arc in the high frequency region and a small diameter arc in the low frequency region. These two arcs represent the charge and mass transfer resistances, respectively. The intercept of the large diameter arc at the high frequency region represents the ohmic resistance ( $R_{\text{ohmic}}$ ) and values of  $\sim 0.080 \Omega \text{ cm}^2$  and  $\sim 0.078$  were recorded for the PtCo/VC and PtCo/HNGC-750, respectively. The charge ( $R_{\text{ct}}$ ) and mass transfer ( $R_{\text{mt}}$ ) resistances, as well as the diameter of each arc, for PtCo/HNGC-750, are smaller than those of PtCo/VC. The  $R_{\text{mt}}$  was estimated to be  $0.192$  and  $0.232 \Omega \text{ cm}^2$  for PtCo/HNGC-750 and PtCo/VC, respectively. This implies HNGC-750 enhances the charge and mass transfer during the PEMFC operation. Especially, the honeycomb-like structure of HNGC-750 reduces the mass transfer resistance by  $\sim 17\%$  of the value of VC in order to facilitate  $\text{O}_2$  transport and water balance in the catalyst layer. The estimated resistance values from the EIS profiles are tabulated in Table S8.†

An accelerated durability test (ADT) for carbon support was carried out to assess the stability of the HNGC-X support. The ADT protocol suggested by the US Department of Energy (DOE) consists of a triangular sweep cycle between 1.0 and 1.5 V to mimic the potential change during the start and stop process of

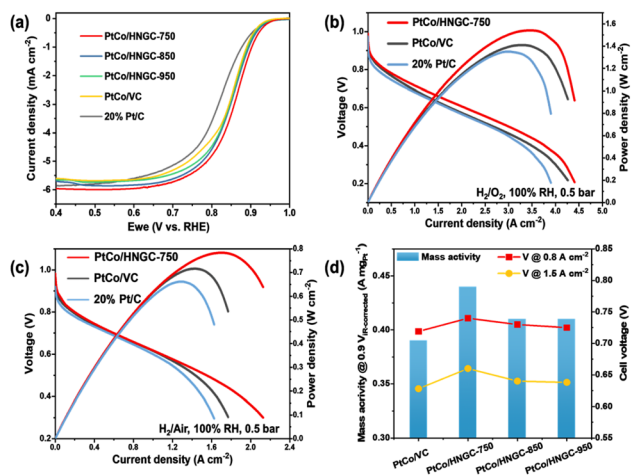


Fig. 4 (a) ORR polarization curves of the samples obtained in  $\text{O}_2$ -saturated  $0.1 \text{ M HClO}_4$  at 1600 rpm. Single cell polarization and power density curves for PtCo/HNGC-750, PtCo/VC, and commercial 20% Pt/C in fully humidified (b)  $\text{H}_2/\text{O}_2$  and (c)  $\text{H}_2/\text{Air}$ . The polarization curves of MEAs were tested with  $0.1 \text{ g}_{\text{PtCo}} \text{ cm}^{-2}$  of cathode loading at  $80^\circ \text{C}$  and backpressure as 0.5 bar. (d) Mass activity at  $0.9 V_{\text{IR-corrected}}$  and cell voltage at 0.8 and  $1.5 \text{ A cm}^{-2}$  for PtCo/VC and PtCo/HNGC-X calculated from the polarization curves under  $\text{H}_2/\text{O}_2$  and ICP-OES results for Pt amount in Table S5.†

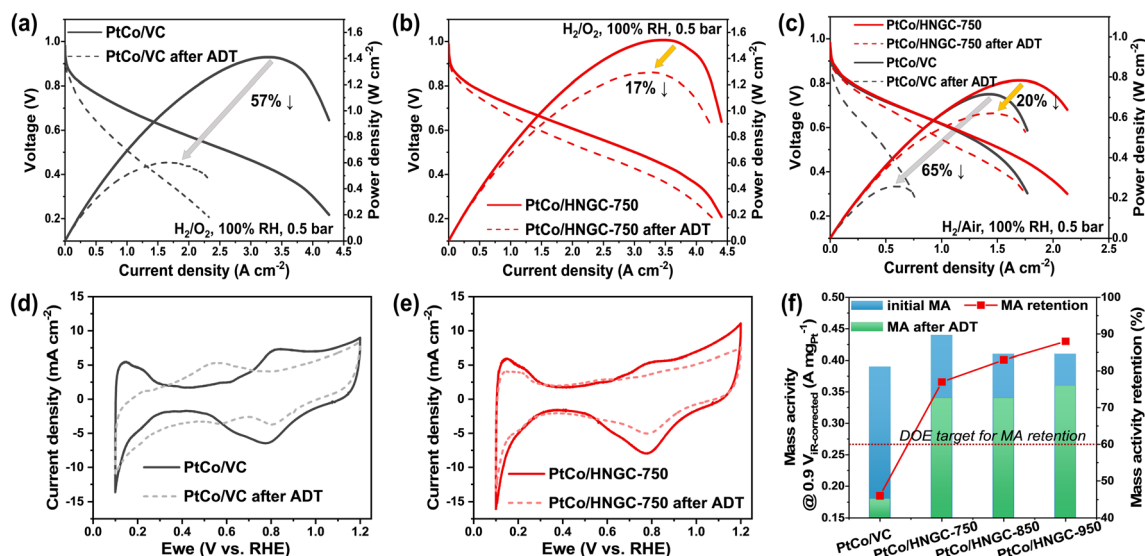


Fig. 5 Single cell polarization and power density curves in fully humidified  $\text{H}_2/\text{O}_2$  for (a) PtCo/VC and (b) PtCo/HNGC-750 before and after 5k cycles of accelerated durability test (ADT) for carbon support durability. (c) Single cell polarization and power density curves for PtCo/HNGC-750 and PtCo/VC before and after 5k cycle ADT results in  $\text{H}_2/\text{Air}$ . The polarization curves of MEAs were tested with  $0.1 \text{ g}_{\text{PtCo}} \text{ cm}^{-2}$  of cathode loading at 80 °C and backpressure as 0.5 bar. Cyclic voltammetry curves for (d) PtCo/VC and (e) PtCo/HNGC-750 before and after ADT were obtained at 80 °C under fully humidified  $\text{H}_2/\text{N}_2$  flow in ambient pressure. (f) Mass activity (MA) at 0.9  $V_{\text{R-corrected}}$  and MA retention for PtCo/VC and PtCo/HNGC-X from the polarization curves under  $\text{H}_2/\text{O}_2$ .

practical fuel cells (Fig. S14a†).<sup>38</sup> PtCo/HNGC-750 exhibits excellent durability compared to PtCo/VC. In Fig. 5a and b,  $P_{\text{max}}$  of PtCo/HNGC-750 only drops by 17%, while PtCo/VC loses 57% of its initial  $P_{\text{max}}$ . PtCo/HNGC-750 also demonstrates high durability in  $\text{H}_2/\text{Air}$  conditions (Fig. 5c). The high graphiticity of PtCo/HNGC-750 enhances the stability under the harsh oxidative condition during the ADT. In contrast, the PtCo/VC support decomposed at a faster rate due to its non-graphitized structure. This led to the collapse of the pore structure, a reduction in the electrical conductivity, and the aggregation of metal nanoparticles. The CVs for PtCo/VC in Fig. 5d show no significant H-adsorption peak after ADT owing to the agglomeration of the PtCo particles. The average particle size of PtCo in PtCo/VC increases from 4.1 to 6.4 nm (56%). However, the PtCo/HNGC-750 increases only by 28% of the initial particle size (Fig. S11c and d†). Interestingly, the thickness of the double-layer (0.3–0.7  $V_{\text{RHE}}$ ) increases because the VC is functionalized by oxygen-containing groups after the carbon corrosion, thus, enhancing the capacitive current.<sup>39</sup> In contrast, the double layer region observed for PtCo/HNGC-750 after ADT is almost the same as that of the initial and the electrochemical surface area (ECSA) decreases only by 28% (from 52.4 to 37.7  $\text{m}^2 \text{ g}_{\text{Pt}}^{-1}$ ) as shown in Fig. 5e. This result translates into the mass activity (MA) change observed in Fig. 5f after ADT. The initial MA of PtCo/HNGC-750 satisfies the DOE beginning-of-life (BOL) target (0.44  $\text{A mg}_{\text{Pt}}^{-1}$ ) and decreases by only 23% of its initial MA after ADT. On the other hand, a 54% loss in MA is observed for the PtCo/VC; a performance drastically below the DOE targets. All PtCo/HNGC-X samples meet the MA retention target of DOE (>60%). Thus, the PtCo/HNGC-X could be promising oxidation-resistant carbon support, providing facile ORR kinetics as a result of the

high graphitization, N-doping and unique honeycomb-like porous structure (see Tables S6 and S7†). The carbon support durability tests for PtCo/HNGC-850 and -950 are summarized in Fig. S14b, c and Table S6.† The major observation here shows that as the preparation temperature increases, the corrosion resistance gets significantly enhanced due to the increase in graphiticity.

## Conclusions

In conclusion, graphitized carbon with a honeycomb-like structure was prepared from the annealing of  $\text{g-C}_3\text{N}_4$  with Mg metal. In this novel process, Mg takes N atoms from the  $\text{g-C}_3\text{N}_4$  structure and causes unstable C atoms to generate highly graphitized carbon materials. Interestingly, self-generated  $\text{Mg}_3\text{N}_2$  particles were embedded in the carbon matrix and served as a template for the honeycomb-like morphology. This work is the first of its kind that reports such an *in situ* generated  $\text{Mg}_3\text{N}_2$  porogen. Thus, Mg in this synthesis technique has a dual function of concurrently enhancing graphiticity and porosity in carbon materials. In addition, using  $\text{g-C}_3\text{N}_4$  as a carbon source leads to sufficient N-doping in the HNGC-X substrate. This synthesis strategy simultaneously induces three key features, (graphiticity, porosity, and heteroatom dopants) in carbon materials, through simple low-temperature heat treatment. These unique properties enhanced the catalytic activity of as-synthesized PtCo in PEMFC. Especially, the unique mesoporous structure offers higher performance than the commercial carbon support in the MEA test owing to the facile mass transport. In addition, the durability under the harsh oxidative condition is dramatically increased by the graphitized carbon

structure, satisfying the DOE target in terms of mass activity degradation. Therefore, we envisage that Mg-assisted carbonization with different organics will open the door for further research and advances in electrocatalytic applications.

## Author contributions

Ha-Young Lee: conceptualization, methodology, data curation, investigation, writing – original draft. Caleb Gyan-Barimah: investigation, writing – original draft. Cheol-Hwan Shin: validation, data curation. Jong-Sung Yu: conceptualization, project administration, funding acquisition, writing – review & editing, supervision.

## Conflicts of interest

There are no conflicts to declare.

## Acknowledgements

This work was supported by National Research Foundation (2019R1A2C2086770 and RS-2023-00223196) funded by the Korean government. Authors also would like to thank KBSIs at Daegu and Busan for SEM, TEM and XPS measurements and CCRF in DGIST for SEM measurements.

## Notes and references

- 1 L. Yang, J. Shui, L. Du, Y. Shao, J. Liu, L. Dai and Z. Hu, *Adv. Mater.*, 2019, **31**, e1804799.
- 2 J. W. Zhang, Y. L. Yuan, L. Gao, G. M. Zeng, M. F. Li and H. W. Huang, *Adv. Mater.*, 2021, **33**, 2006494.
- 3 L. Du, V. Prabhakaran, X. Xie, S. Park, Y. Wang and Y. Shao, *Adv. Mater.*, 2021, **33**, e1908232.
- 4 D. H. Guo, R. Shibuya, C. Akiba, S. Saji, T. Kondo and J. Nakamura, *Science*, 2016, **351**, 361–365.
- 5 S. B. Yoon, G. S. Chai, S. K. Kang, J.-S. Yu, K. P. Gierszal and M. Jaroniec, *J. Am. Chem. Soc.*, 2005, **127**, 4188–4189.
- 6 D. B. Schuepfer, F. Badaczewski, J. M. Guerra-Castro, D. M. Hofmann, C. Heiliger, B. Smarsly and P. J. Klar, *Carbon*, 2020, **161**, 359–372.
- 7 S. L. Zhao, D. W. Wang, R. Amal and L. M. Dai, *Adv. Mater.*, 2019, **31**, 1801526.
- 8 D.-S. Yang, D. Bhattacharjya, S. Inamdar, J. Park and J.-S. Yu, *J. Am. Chem. Soc.*, 2012, **134**(39), 16127–16130, 22966761.
- 9 F. Marpaung, M. Kim, J. H. Khan, K. Konstantinov, Y. Yamauchi, M. S. A. Hossain, J. Na and J. Kim, *Asian J. Chem.*, 2019, **14**, 1331–1343.
- 10 Y. J. Wang, D. P. Wilkinson and J. Zhang, *Chem. Rev.*, 2011, **111**, 7625–7651.
- 11 N. Macauley, D. D. Papadias, J. Fairweather, D. Spornjak, D. Langlois, R. Ahluwalia, K. L. More, R. Mukundan and R. L. Borup, *J. Electrochem. Soc.*, 2018, **165**, F3148–F3160.
- 12 J. Zhao, Z. Tu and S. H. Chan, *J. Power Sources*, 2021, **488**, 2294934.
- 13 C. A. Reiser, L. Bregoli, T. W. Patterson, J. S. Yi, J. D. L. Yang, M. L. Perry and T. D. Jarvi, *Electrochem. Solid-State Lett.*, 2005, **8**, A273–A276.
- 14 H.-Y. Lee, T. H. Yu, C.-H. Shin, A. Fortunelli, S. G. Ji, Y. Kim, T.-H. Kang, B.-J. Lee, B. V. Merinov, W. A. Goddard, C. H. Choi and J.-S. Yu, *Appl. Catal., B*, 2023, **323**, 122179.
- 15 E. Negro, K. Vezzu, F. Bertasi, P. Schiavuta, L. Toniolo, S. Polizzi and V. Di Noto, *Chemelectrochem*, 2014, **1**, 1359–1369.
- 16 M. Borghei, N. Laocharoen, E. Kibena-Poldsepp, L. S. Johansson, J. Campbell, E. Kauppinen, K. Tammeveski and O. J. Rojas, *Appl. Catal., B*, 2017, **204**, 394–402.
- 17 V. Perazzolo, R. Brandiele, C. Durante, M. Zerbetto, V. Causin, G. A. Rizzi, I. Cerri, G. Granozzi and A. Gennaro, *ACS Catal.*, 2018, **8**, 1122–1137.
- 18 B.-A. Lu, L.-F. Shen, J. Liu, Q. Zhang, L.-Y. Wan, D. J. Morris, R.-X. Wang, Z.-Y. Zhou, G. Li, T. Sheng, L. Gu, P. Zhang, N. Tian and S.-G. Sun, *ACS Catal.*, 2020, **11**, 355–363.
- 19 B. Fang, J. H. Kim, M. S. Kim and J.-S. Yu, *Acc. Chem. Res.*, 2013, **46**, 1397–1406.
- 20 N. Díez, M. Sevilla and A. B. Fuertes, *Carbon*, 2021, **178**, 451–476.
- 21 X. Y. Zhang, S. Zhang, Y. Yang, L. G. Wang, Z. J. Mu, H. S. Zhu, X. Q. Zhu, H. H. Xing, H. Y. Xia, B. L. Huang, J. Li, S. J. Guo and E. K. Wang, *Adv. Mater.*, 2020, **32**, 1906905.
- 22 T. Morishita, T. Tsumura, M. Toyoda, J. Przepiorski, A. W. Morawski, H. Konno and M. Inagaki, *Carbon*, 2010, **48**, 2690–2707.
- 23 Y. Ding, C. Yu, J. Chang, C. Yao, J. Yu, W. Guo and J. Qiu, *Small*, 2020, **16**, e1907164.
- 24 C.-H. Shin, T. H. Yu, H.-Y. Lee, B.-J. Lee, S. Kwon, W. A. Goddard and J.-S. Yu, *Appl. Catal., B*, 2023, **334**(5), 122829.
- 25 K. V. Kumar, S. Gadipelli, B. Wood, K. A. Ramisetty, A. A. Stewart, C. A. Howard, D. J. L. Brett and F. Rodriguez-Reinoso, *J. Mater. Chem. A*, 2019, **7**, 10104–10137.
- 26 P. Qiu, H. Chen, C. Xu, N. Zhou, F. Jiang, X. Wang and Y. Fu, *J. Mater. Chem. A*, 2015, **3**, 24237–24244.
- 27 Y. Hao, Y. Wang, L. Wang, Z. Ni, Z. Wang, R. Wang, C. K. Koo, Z. Shen and J. T. Thong, *Small*, 2010, **6**, 195–200.
- 28 S. Ott, F. Du, M. L. Luna, T. A. Dao, S. Selve, B. R. Cuenya, A. Orfanidi and P. Strasser, *Appl. Catal., B*, 2022, **306**, 121118.
- 29 M. Wu, J. M. Yan, X. N. Tang, M. Zhao and Q. Jiang, *ChemSusChem*, 2014, **7**, 2654–2658.
- 30 C.-H. Shin, H.-Y. Lee, C. Gyan-Barimah, J.-H. Yu and J.-S. Yu, *Chem. Soc. Rev.*, 2023, **52**, 2145–2192.
- 31 E. Luo, M. Xiao, J. Ge, C. Liu and W. Xing, *J. Mater. Chem. A*, 2017, **5**, 21709–21714.
- 32 C. H. Wang, J. Kim, J. Tang, M. Kim, H. Lim, V. Malgras, J. You, Q. Xu, J. S. Li and Y. Yamauchi, *Chem*, 2020, **6**, 19–40.
- 33 M. Kim, K. L. Firestein, J. F. S. Fernando, X. T. Xu, H. Lim, D. V. Golberg, J. Na, J. Kim, H. Nara, J. Tang and Y. Yamauchi, *Chem. Sci.*, 2022, **13**, 10836–10845.
- 34 W. Ding, Z. Wei, S. Chen, X. Qi, T. Yang, J. Hu, D. Wang, L. J. Wan, S. F. Alvi and L. Li, *Angew. Chem., Int. Ed. Engl.*, 2013, **52**, 11755–11759.

- 35 B. Y. Xia, H. B. Wu, N. Li, Y. Yan, X. W. Lou and X. Wang, *Angew. Chem., Int. Ed. Engl.*, 2015, **54**, 3797–3801.
- 36 E. B. Tetteh, C. Gyan-Barimah, H.-Y. Lee, T.-H. Kang, S. Kang, S. Ringe and J.-S. Yu, *ACS Appl. Mater. Interfaces*, 2022, **14**(22), 25246–25256, 35609281.
- 37 S. Ott, A. Bauer, F. Du, T. A. Dao, M. Klingenhof, A. Orfanidi and P. Strasser, *ChemCatChem*, 2021, **13**, 4759–4769.
- 38 U.S. Department of Energy (DOE), *Fuel Cell Technologies Office, (FCTO) Fuel Cells Multi-Year Research Development and Demonstration Plan, Table P.1 and P.2*, [https://www.energy.gov/sites/prod/files/2016/06/f32/fcto\\_myrrdd\\_fuel\\_cells\\_0.pdf](https://www.energy.gov/sites/prod/files/2016/06/f32/fcto_myrrdd_fuel_cells_0.pdf), 2016, (accessed 28 March 2023).
- 39 P. Kanninen, B. Eriksson, F. Davodi, M. E. M. Buan, O. Sorsa, T. Kallio and R. W. Lindstrom, *Electrochim. Acta*, 2020, **332**, 135384.